ARTICLE

Temperature-dependent sensitivity enhancement of solid-state NMR spectra of α-synuclein fibrils

Kathryn D. Kloepper · Donghua H. Zhou · Ying Li ·
Kem A. Winter · Julia M. George · Chad M. Rienstra

Abstract The protein α-synuclein (AS) is the primary fibrillar component of Lewy bodies, the pathological hallmark of Parkinson's disease. Wild-type human AS and the three mutant forms linked to Parkinson's disease (A53T, A30P, and E46K) all form fibrils through a nucleation-dependent pathway; however, the biophysical details of these fibrillation events are not yet well understood. Atomic-level structural insight is required in order to elucidate the potential role of AS fibrils in Parkinson's disease. Here we show that low temperature acquisition of magic-angle spinning NMR spectra of wild type AS fibrils greatly enhances spectral sensitivity, enabling the detection of a substantially larger number of spin systems. At $0 \pm 3°C$ sample temperature, cross polarization (CP) experiments yield weak signals. Lower temperature spectra ($-40 \pm 3°C$) demonstrated several times greater signal intensity, an effect further amplified in 3D $^{15}N–^{13}C–^{13}C$ experiments, which are required to perform backbone assignments on this sample. Thus 3D experiments enabled assignments of most amino acids in the rigid part of the fibril (approximately residues 64 to 94), as well as tentative site-specific assignments for T22, V26, A27, Y39, G41, S42, H50, V52, A53, T54, V55, V63, A107, I112, and S129. Most of these signals were not observed in 2D or 3D spectra at $0 \pm 3°C$. Spectra acquired at low temperatures therefore permitted more complete chemical shift assignments. Observation of the majority of residues in AS fibrils represents an important step towards solving the 3D structure.

Keywords Magic-angle spinning · Amyloid · Protein structure · Chemical shift assignments · Multidimensional · Parkinson's disease

K. D. Kloepper · D. H. Zhou · K. A. Winter ·
C. M. Rienstra (✉)
Department of Chemistry, University of Illinois at Urbana-Champaign, 600 South Mathews Avenue, Urbana, IL 61801, USA
e-mail: rienstra@scs.uiuc.edu

Y. Li · C. M. Rienstra
Center for Biophysics and Computational Biology, University of Illinois at Urbana-Champaign, Urbana, IL 61801, USA

J. M. George
Department of Molecular and Integrative Physiology, University of Illinois at Urbana-Champaign, Urbana, IL 61801, USA

C. M. Rienstra
Department of Biochemistry, University of Illinois at Urbana-Champaign, Urbana, IL 61801, USA

Introduction

α-Synuclein (AS), a 140-residue brain protein, is the primary fibrillar component of Lewy bodies, the pathological hallmark of Parkinson's disease (PD) (Spillantini et al. 1997). Additionally, three single-point mutations (A53T, A30P, and E46K) have been implicated in hereditary PD (Kruger et al. 1998; Polymeropoulos et al. 1997; Zarranz et al. 2004). AS is unstructured in solution, and it has been demonstrated to aggregate into fibrils with cross-β secondary structure as characterized by x-ray and electron diffraction (Conway et al. 2000; Serpell et al. 2000), but atomic-resolution structural information is limited. The central hydrophobic region of residues ~ 60 to ~ 95 has been shown to be crucial for AS fibrillation (Iwai et al. 1995). Protease digestion of AS fibrils demonstrated that residues 31–101 are protease resistant (Miake et al. 2002); recent hydrogen exchange experiments demonstrated that residues 39–101 are protected (Del Mar et al. 2005).

Likewise, EPR studies on site-directed spin-labeled AS fibrils reveal a well-ordered central region (34–101) with parallel, in-register β-strands (Der-Sarkissian et al. 2003). Despite these advances towards an AS fibril structure, the molecular mechanisms of fibrillation and its roles in the etiology of PD are not known. An enhanced understanding of AS fibril structure at atomic resolution will provide important fundamental biochemical information and possibly elucidate the roles that AS fibrils play in the pathogenesis of PD.

Fibrils are not amenable to study by the traditional structural techniques of x-ray crystallography or solution NMR. In recent years, solid-state NMR (SSNMR) has emerged as a powerful technique for examination of atomic-resolution structure of microscopically ordered samples; complete de novo structures of several small proteins have now been reported by multidimensional magic-angle (MAS) SSNMR methods (Castellani et al. 2002; Lange et al. 2005; Zech et al. 2005). SSNMR has been applied successfully to β-amyloid fibrils (Balbach et al. 2000, 2002; Benzinger et al. 1998, 2000; Lansbury et al. 1995). Extensive studies of selectively labeled amyloid peptides resulted in an atomic-resolution structural model of β-amyloid (Petkova et al. 2002), which was extended with further experimental data, including more precise measurements of internuclear distances (Petkova and Tycko 2004) to produce a refined model (Petkova et al. 2006). More recently, other amyloidogenic peptides have been examined with multidimensional methods, including a series of detailed studies of the HET-s prion (Ritter et al. 2005; Siemer et al. 2005, 2006a, b) and a recent report demonstrating the first site-resolved spectra of full-length, WT AS fibrils obtained with uniformly-^{13}C,^{15}N-labeled samples (Heise et al. 2005).

A remaining challenge in structural studies of fibrillar proteins by SSNMR is to identify, resolve, and assign all the signals throughout larger protein domains. This requires improved spectral sensitivity without compromising resolution. We have previously developed a high-yield expression and purification protocol for isotopically labeled AS (Kloepper et al. 2006) and published preliminary SSNMR spectra of the disease-relevant A30P AS fibrils using new 3D methods developed in our laboratory (Zhou et al. 2006).

Here we show that wild type AS fibrils yield spectra with improved sensitivity as sample temperature is lowered from 0 to –40°C. This effect is fully reversible. The enhanced sensitivity permits acquisition of 3D correlation spectra at –40°C with a substantially larger number of spin systems observed than at 0°C. The improved data quality enables more complete chemical shift assignment of the fibril core and site-specific secondary structure analysis of

turns and loops that are not detected at 0°C by experiments based on dipolar transfer.

Materials and methods

Sample preparation

Uniformly-^{13}C,^{15}N-labeled wild-type AS was expressed and purified as previously described (Kloepper et al. 2006). Immediately prior to incubation, AS solutions were passed through a 0.22 μm filter to remove any pre-formed fibrils. Fibrils used as seeds for subsequent fibrillation experiments were prepared by incubating 1 mM AS in fibrillation buffer (0.10 mM EDTA, 0.02% NaN$_3$ (w/v), and 50 mM Na phosphate buffer, pH 7.4) at 37°C with agitation at 250 rpm. After three weeks, the fibrils were separated from solution by centrifugation at 100,000g for 1 h. The OD$_{280}$ of the supernatant was consistent with a lack of monomeric AS, confirming quantitative conversion of all AS into AS fibrils. Fibril pellets were packed directly into 4.0 mm NMR rotors for analysis (Varian, Inc., Palo Alto, CA). The sample was confined to the active sample region of the rotor and sealed with Kel-F spacers and rubber discs (Franks et al. 2005). The packed rotor was weighed before and after NMR experiments to confirm that the sample remained fully hydrated; changes in mass were less than the uncertainty in the measurement (±1 mg).

After NMR experiments, the pellets were recovered from the NMR rotor and resuspended in 50 mM phosphate buffer. Subsequent fibril preparations were seeded with 1% pre-formed fibrils to ensure reproducibility of fibril morphology, as demonstrated for β-amyloid (Petkova et al. 2005). Seeded solutions of AS were placed into microtubes (Eppendorf), purged, sealed, and incubated at 37 °C with agitation for 1–2 weeks. Fibrils were centrifuged and packed into NMR rotors as described above. Rotors were stored at –20°C between NMR experiments, which were conducted with temperatures ranging from 0 to –60°C. Under these conditions, AS fibril samples are stable for over 18 months.

NMR experiments

Spectra were acquired on Varian InfinityPlus four-channel spectrometers, using a T3 ^{1}H-^{13}C-^{15}N 4.0-mm probe at 8.333 kHz spinning rate for 500 MHz experiments, and a custom-designed prototype Varian Balun^{TM} ^{1}H-^{13}C-^{15}N 4.0 mm probe at 10 kHz spinning rate for 600 MHz experiments. The variable temperature gas was maintained as indicated in figure captions with 90 ± 10 scfh flow rate; temperatures reported are the effective mean sample

temperature, which have an error of ±3 °C, as determined by methanol calibration (Van Geet 1968). Chemical shifts were referenced externally with adamantane (Morcombe and Zilm 2003). Temperature-dependent 1D spectra were acquired three ways: direct polarization, cross polarization, and a summation of the two. Direct polarization (DP) spectra were acquired with a pulse delay at least two times the ^{13}C T_1 value (typically 5 s unless noted otherwise), with a single $\pi/2$ pulse on ^{13}C and TPPM decoupling on ^{1}H (Bennett et al. 1995). Cross polarization (CP) spectra (Pines et al. 1973) were acquired with a $\pi/2$ pulse (3.0 μs) on ^{1}H followed by a constant-amplitude spin lock ($\sim$60 kHz), matched to a Hartmann-Hahn condition (Hartmann and Hahn 1962) under MAS conditions (Schaefer and Stejskal 1976) with the ^{13}C field set to slightly less than ^{1}H (e.g., $\sim$50 kHz for 10 kHz MAS). Tangent ramps were utilized on the ^{13}C channel (Hediger et al. 1995). To obtain quantitative intensities for CP only, spin temperature alternation of the ^{1}H $\pi/2$ pulse was performed, relative to the ^{13}C spin lock field. Alternatively, to maximize signal intensity for 2D and 3D experiments, the DP and CP signals were added together experimentally by applying the $\pi/2$ pulse on ^{13}C prior to ^{1}H-^{13}C CP, where the ^{13}C spin lock field was along the axis of the ^{13}C signal after the $\pi/2$ pulse (i.e. the ^{13}C spin lock phase was always 90° less than the $\pi/2$ pulse phase); in this case, spin temperature alternation of the ^{1}H $\pi/2$ pulse was not performed. We refer to this spectrum as "DPCP", to indicate that the direct and cross polarized signals are both observed in the same spectrum. A similar strategy was employed for all 2D and 3D experiments to enhance sensitivity (Rienstra et al. 2000). $T_{1\rho}$ measurements were performed with CP experiment, varying the timing of an additional ^{1}H spin lock pulse timing between the $\pi/2$ and ^{13}C spin lock pulses (for the ^{1}H measurement), or varying the time of an additional spin lock pulse on ^{13}C after the HC CP period. T_1 measurements were performed with standard inversion recovery experiments; in the case of ^{1}H, the T_1 values are reported by detecting the ^{13}C signal after CP.

Two-dimensional CC spectra were acquired at 600 MHz ^{1}H frequency using DARR (Takegoshi et al. 2001) (RAD) (Morcombe et al. 2004) mixing at the $n = 1$ rotary resonance condition on the ^{1}H channel ($\omega_H = \omega_R$), with the indirect dimension digitized to 768 real (TPPI) (Marion and Wüthrich 1983) points, a 10 μs dwell time (for a 7.68 ms maximum evolution time, or 1.0 ppm digital resolution), and 2048 complex points in the direct dimension with a 10 μs dwell time (0.4 ppm digital resolution). Mixing times and temperatures, along with any variations from these default parameters, are indicated in each figure caption.

Triple resonance NCOCX, NCACX and CANCO and CCC experiments were performed at 10 kHz MAS rate, 600 MHz ^{1}H frequency using pulse sequences and conditions described previously (Franks et al. 2005; Frericks

et al. 2006; Li et al. 2006; Li et al. 2007; Zhou et al. 2006) with TPPI (real) sampling of indirect dimensions. In all cases reference spectra (equivalent to the first row of each experiment, but with 64 or 128 scans) were acquired periodically throughout the 3D data acquisition and showed less than 2% variation in the overall signal intensity.

The NCACX 3D experiment was acquired with 1 ms HN CP, 80×150 μs evolution in t_1 (N), 6 ms SPECIFIC CP (Baldus et al. 1998) for NCA transfer with $\omega_N = 5/2 \ \omega_R$, $\omega_C = 3/2 \ \omega_R$ and $\sim$95 kHz CW ^{1}H decoupling, 96×50 μs evolution in t_2 (CA), 10 ms CC mixing with DARR (Morcombe et al. 2004; Takegoshi et al. 2001), and 2048×10 μs acquisition (CX); TPPM decoupling (6.3 μs, 15°, 75 kHz nominal nutation frequency on ^{1}H) was used in all chemical shift evolution and acquisition periods. A total of 7,680 rows with 8 scans per row and a pulse delay of 1.25 s resulted in a total experiment time of 21 h. The entire experiment was performed twice and co-added for a total of 42 h of measurement time.

The NCOCX 3D experiment was acquired with 1 ms HN CP, 80×150 μs evolution in t_1 (N), 5 ms SPECIFIC CP for NCO transfer with $\omega_N = 5/2 \ \omega_R$, $\omega_C = 7/2 \ \omega_R$ and $\sim$90 kHz CW ^{1}H decoupling, 32×150 μs evolution in t_2 (C'), 15 ms DARR mixing, and 2048×10 μs acquisition (CX), with the TPPM decoupling (6.3 μs, 15°) in all free evolution periods. This experiment in total consisted of 2,560 rows, 8 scans per row, 1.25 s pulse delay, for 7 h per block. The entire experiment was repeated 5 times for a total of 35 h acquisition.

The CANCO experiment was acquired with 0.35 ms HC transfer, 80×100 μs evolution in t_1 (CA), 4.5 ms CAN transfer under 95 kHz ^{1}H decoupling and the NCA CP condition noted above for the NCACX experiment, 50×200 μs evolution in t_2 (N), 7.2 ms NCO transfer with the conditions noted above for the NCOCX experiment and 1536×10 μs acquisition time. This experiment required a total of 4,000 rows, 4 scans per row, 3 s pulse delay, for a total of 13.5 h per block, with 7 blocks for a total of 95 h measurement time. (The pulse delay for this experiment was set to an unnecessarily long value by accident; equally good data could have been acquired in $\sim$42 h.)

The CCC 3D experiment (Zhou et al. 2006) was acquired with 0.5 ms HC CP, 60×50 μs evolution in t_1, soft-pulse coherence selection of the aliphatic region of the spectrum prior to 25 ms mixing (DARR), 80×14.4 μs evolution in t_2, 100 ms DARR mixing, and 1536×10 μs acquisition. TPPM decoupling parameters were 5.8 μs and 15° with a nominal 80 kHz ^{1}H nutation frequency. This experiment was performed with 8 scans per row, 1.5 s pulse delay, 4,800 rows for a total of 16 h per experiment, repeated five times for a total acquisition of 80 h.

Data were processed with nmrPipe (Delaglio et al. 1995) with back linear prediction and polynomial baseline
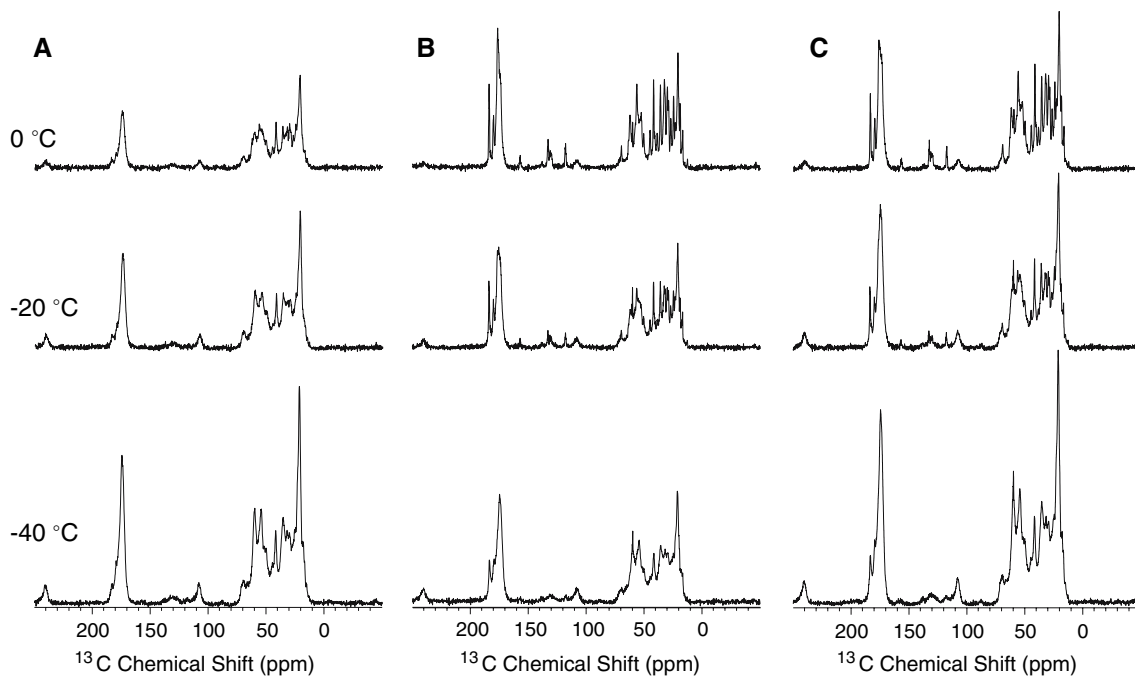
Fig. 1 Comparison of ^{13}C 1D spectra of AS fibrils acquired as a function of temperature. (**A**) cross polarization, (**B**) direct polarization, and (**C**) direct and cross polarization. 128 scans each, 500 MHz ^{1}H frequency

(frequency domain) correction applied to the direct dimension. When indicated, Lorentzian-to-Gaussian apodization was applied with a ratio of 1:3 Lorentzian line narrowing to Gaussian line broadening, resulting in a net line broadening but relative narrowing of the base of the lineshape in comparison to pure Lorentzian, which enhances the appearance of 2D spectra. Each dimension of time-domain data was zero filled at least once (to a minimum of 2048 × 4096 complex points for 2D spectra, or 256 × 256 × 2048 points for 3D spectra). Cosine bells (phase shifted +20°) were employed for processing of the indirect dimensions of the 3D spectra, which were acquired with shorter evolution times than the 2D spectra. Additional details for each spectrum are found in the respective figure captions. Peak heights, signal-to-noise ratios, and linewidths were calculated in Sparky (Goddard and Kneller 2006) using Gaussian peak integration methods. Secondary structure analysis of the Ala CA-CB crosspeaks was performed as reported previously (Frericks et al. 2006).

Results and discussion

Temperature-dependent cross-polarization dynamics

One-dimensional ^{13}C MAS spectra of AS fibrils acquired at 0°C have overall peak intensity patterns and linewidths consistent with a microscopically well-ordered solid

peptide (Fig. 1). However, the signal intensity of AS fibrils was substantially lower than expected based on the quantity of protein, which we investigated further by acquiring DP, CP, and DPCP spectra over a range of temperatures. The CP spectrum at 0°C demonstrated much lower signal intensity and numbers of signals than expected for the 140-residue protein (Fig. 1A). Compared with the total integrated intensity observed in spectra of other microcrystalline proteins of known quantity, including ubiquitin (Igumenova et al. 2004) and GB1 (Franks et al. 2005), at this condition AS had an integrated intensity only 40% of the expected value. This corresponds to a difference of a factor of 2.5, which is the typical ^{1}H-^{13}C cross polarization (CP) enhancement that we observe for microcrystalline proteins. In contrast, the CP enhancement factor for AS was ∼0.7 (Fig. 1A–B). Comparable values were obtained on different probes, on both 500 and 600 MHz spectrometers. Fig. 1C shows the spectrum including both the DP and CP components (DPCP, as described in Materials and Methods), which we performed in order to maximize the sensitivity at 0°C. The patterns of peaks observed in the DP and DPCP spectra include well resolved downfield Glu CD1 (184 ppm), Tyr CZ (157.5 ppm), Thr CB (70–72 ppm), Gly CA (44–47 ppm), and Ile CD1 (13 ppm); these appear with especially high resolution, in some cases demonstrating resolution of fine structure from the ^{13}C-^{13}C scalar couplings, which range from ∼35 Hz (Ile CD1-CG1) to 67 Hz (Tyr CZ-CE).

Several of these signals are much weaker in the CP spectra at 0°C. The sharp peaks observed in DP most likely arise from mobile segments of the molecule with their motion rendering CP very inefficient.

We investigated the CP enhancement factor over a range of temperatures, observing a substantial increase in signal intensity as the temperature was decreased. For example, in the DPCP spectra (Fig. 1C) the carbonyl (185 to 170 ppm) and methyl (25 to 10 ppm) regions increase by 40% and 49% respectively, and new aliphatic peaks appear as temperature is decreased to –40°C. Between –8 and –16°C, three concerted events occurred: (1) the probe tuning changed substantially (an effect observed on multiple probes); (2) the water signal observed in 1D ^{1}H spectra was attenuated by an order of magnitude; (3) the phase of the water signal in this spectrum changed significantly. We attribute these observations to freezing of the mother liquor. In contrast to these rapid changes of the mother liquor phase behavior, the changes in signal intensity of the protein were far more gradual. A substantial fraction of the change in intensity occurred as the temperature was lowered to –20°C, with an increase in intensity of 48% (relative to 0°C). An additional 29% increase was observed between –20°C and –40°C, and finally a 16% increase from –40°C to –60°C. In total, a 123% increase in signal intensity in the DPCP-MAS spectrum was observed as temperature was decreased from 0 to –60°C, which appeared to plateau at the lower end of this range. Since this is also the range of temperatures over which extended 2D and 3D experiments can currently be performed on this instrument, we restricted further study to this regime.

The increased intensity was derived primarily from the CP signal, since the DP intensity is essentially constant over the temperature range studied (note that all spectra in Fig. 1 are plotted at the same absolute scale). To investigate the origin of the increase in CP enhancement, we acquired ^{1}H-^{13}C dipolar dephasing curves with the R18$_1^7$ sequence (Zhao et al. 2001) at several conditions (Fig. 2). The dipolar dephasing of the DP spectrum at 0°C shows a very shallow, slow modulation, consistent with high mobility (a low average backbone order parameter). The CP spectrum at 0°C demonstrates a fractional dephasing due to the fact that CP filters for the rigid portions of sample; nevertheless, the initial oscillation of this dephasing curve is less than half of the dephasing amplitude expected for a CA site in the rigid lattice limit. As temperature is lowered, the extent of dephasing increases significantly, approaching the result expected for a rigid lattice backbone site as the sample temperature approaches –40°C. The dephasing trajectories approximate the ^{1}H-^{13}C CP dynamics, with conditions where low order parameters are observed, correlating to the poor CP efficiency. In experiments involving multiple dipolar transfers, such as
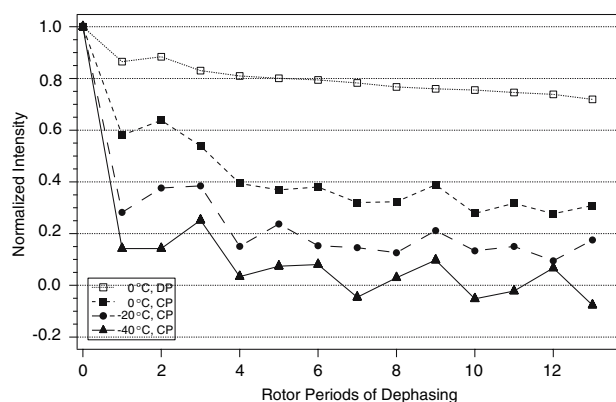

Fig. 2 ^{1}H-^{13}C dipolar dephasing curves acquired with R18$_1^7$ sequence (Zhao et al. 2001). Data were acquired with direct polarization at 0°C (open squares); with cross polarization at 0°C (filled squares); with cross polarization at –20°C (filled circles); with cross polarization at –40°C (filled triangles)

^{1}H-^{13}C-^{13}C or ^{1}H-^{15}N-^{13}C-^{13}C pathways, the efficiency losses are amplified, as observed in the relative sensitivity of 2D and 3D experiments discussed further below. An additional contribution to the observed CP efficiency variation is the ^{13}C $T_{1\rho}$, which for the carbonyl region, for example, was 9.9 ms at 0°C, 8.1 ms at –20°C and 11.8 ms at –40°C. This difference is expected to have an additional contribution to the N-CO transfer efficiency especially when optimal N-CO mixing times are on the order of 6 to 8 ms, comparable to the $T_{1\rho}$ value.

Temperature-dependent spectral resolution

Upon first inspection, the 1D ^{13}C CP-MAS spectra appear to suffer from deterioration in resolution at lower temperatures. There are three possible explanations for this observation. First, monomeric AS present in the mother liquor may contribute to random coil chemical shifts, as reported in a previous SSNMR AS study (Heise et al. 2005); these signals in CP-MAS experiments would be expected to appear with significant intensity only at temperatures below the macroscopic phase transition. Second, individual resonance lines may broaden due to either homogeneous or inhomogeneous mechanisms. Third, signals that are not present in the 0 °C spectra may appear at lower temperatures, leading to an increase in overlap in the 1D spectrum, which gives the appearance of lower resolution when in fact the individual linewidths may not have changed.

We first addressed the issue of whether monomeric AS was present in the fibril samples. Because monomeric AS is unfolded, upon freezing, if monomeric AS were present in the fibril samples, significant increases in the percentage of numbers of signals with random coil chemical shifts

(corresponding to the unfolded monomer) would be expected. These signals were observed in scalar-mediated transfer experiments in the earlier study. We did not observe such signals for any amino acids with well-resolved spectral signatures (including Gly, Ala, Val, Thr, Ser, and Ile) in ^{13}C DPCP-MAS spectra (Fig. 1C). Furthermore, thioflavin T fluorescence measurements, sedimentation analysis (by mass), and the optical absorbance at 280 nm of the supernatant are all consistent with essentially quantitative conversion of AS to the fibril form. As demonstrated further below, analysis of secondary structure by chemical shift analysis of the solid samples also directly shows only minor (but statistically significant) changes in overall secondary structure, consistent again with a lack monomer in our samples. While it is certainly possible that there is interconversion between monomer and fibril in vivo, at least in the NMR rotor, once AS fibrillates, it remains as a stable fibril. Therefore we conclude that in our experiments the presence of monomeric AS is unlikely to account for the changes in spectra as a function of temperature.

To clarify which of the two remaining phenomena is more prominent in the case of AS fibrils, we performed 2D CC experiments over the same temperature range. The trend of increasing signal intensity at lower temperature is especially apparent in the 2D spectra (Fig. 3). Even in the 2D spectra, because AS has 140 residues, significant portions of the CA-CB region are overlapped. However, among certain residue types, such as Thr, Ala, Val, and Ser, individual peaks are resolved, with increasing intensity at lower temperature (Fig. 4). Of the 19 Ala in AS, only half of the expected CA-CB cross peaks are present at 0°C, but all are observed at –40°C (as verified by 3D experiments where peaks were overlapped in the CC 2D). Relatively few Thr/Ser CB-CA crosspeaks were observed at 0°C, but again all are present at –40°C. Only a fraction of the Val CA-CB peaks are observed at 0°C, while all are recovered

at lower temperatures. The 2D spectra illustrate that not only do new peaks appear; in addition, peaks observed at the high end of the temperature range (e.g., Ala CA-CB cross peaks present at 0°C) continue to increase significantly in intensity at –40°C. For example, the relative integrated intensity of A53 increases by nearly three-fold as temperature is lowered from 0 to –40°C. Likewise, S42 increases in signal intensity by a factor of two.

Resolved peaks in the 2D spectra were used to assess possible changes in linewidths as a function of temperature and supplemented with additional measurements from 3D NCACX and NCOCX spectra. The majority of the peaks observed at each sample temperature did not demonstrate significant line broadening at the lower temperatures. Overall at –40°C, among the 25 representative peaks measured in the NCC 3Ds, the linewidths were 0.52 ± 0.22 ppm in the ^{13}C dimensions and 0.88 ± 0.23 ppm for ^{15}N (where the values reported correspond to the measured linewidths adjusted for the amount of line broadening added during data processing). The larger ^{15}N linewidths are attributable to the inferior digital resolution of the ^{15}N dimension in the 3D spectra, as well as an empirical observation of shorter T_2 values for ^{15}N under these decoupling conditions (perhaps due to the larger CSA of the amide proton, contributing to residual coupling at the relatively high B_0 field used here). Notably in these uniformly-^{13}C-labeled samples, a significant fraction of this total linewidth is due to the scalar ^{13}C-^{13}C couplings. For the majority of peaks observed at both 0°C and –40°C, linewidths typically remained constant within 0.15 ppm. Representative changes in linewidths include G73 CA-C′ (0.40 to 0.55 ppm), A53 CA-CB (0.50 to 0.60 ppm) and S42 CB-CA (0.60 to 0.65 ppm). For several of the crosspeaks observed at both 0 and –40°C, linewidths actually improve slightly at lower temperatures. For example, the linewidth of the A78 CA-CB crosspeak decreases from 0.7 to 0.5 ppm (with a six-fold increase in intensity) in the

Fig. 3 2D ^{13}C-^{13}C spectra acquired with 10 ms DARR mixing, aliphatic region. (**A**) 0°C. (**B**) –40°C. Experiment time was 9 h, and all spectra were processed identically, with net Lorentzian to Gaussian line broadening of 0.13 ppm and 0.20 ppm in the indirect and direct dimensions, respectively
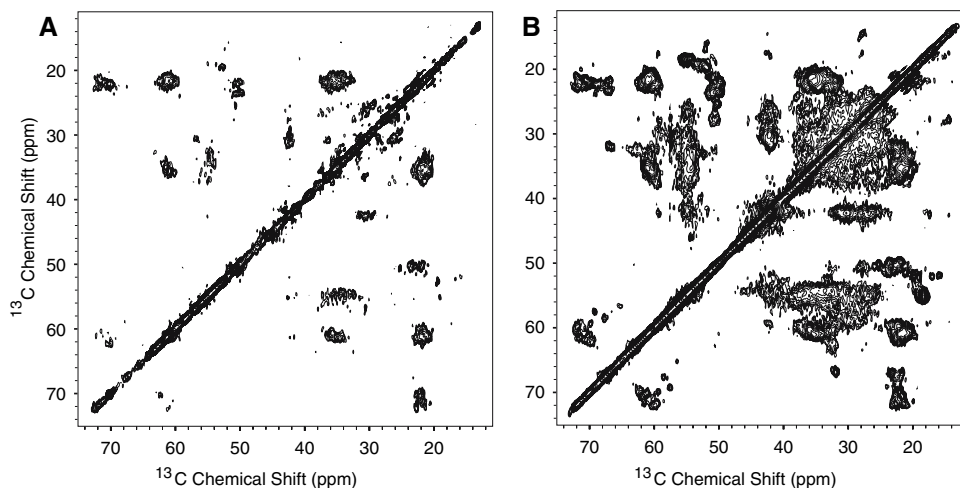
Fig. 4 Expansion of regions of 2D CC spectra acquired as a function of temperature. (**A–C**) Ala CA-CB region at 0, –20 and –40°C; (**D–F**) Ser and Thr CB-CA region at 0, –20 and –40°C; (**G–I**) Val CA-CB region at 0, –20 and –40°C (Pro CA-CB peaks also appear in this direct dimension as temperature is lowered from 0 to –40°C.) Experiment time was 9 h, and all spectra were processed identically, with net Lorentzian to Gaussian line broadening of 0.16 ppm and 0.20 ppm in the indirect and direct dimensions, respectively
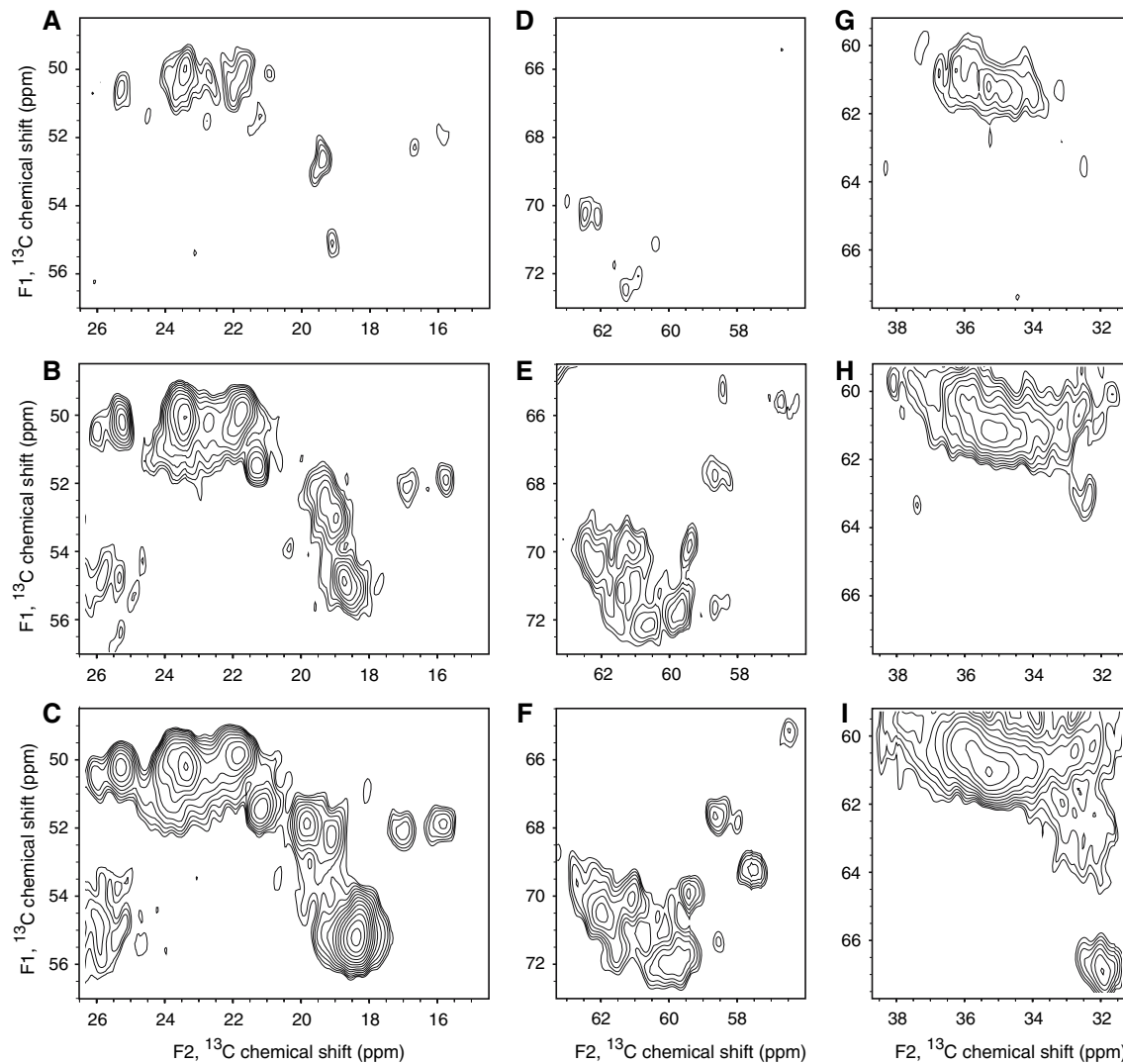
direct dimension as temperature is lowered from 0 to –40°C. Likewise, I88 CD-CG1 narrows from 0.7 to 0.5 ppm in the direct dimension with a 5-fold increase in intensity. Although the major contribution to the change in intensity of these signals is the CP efficiency, as demonstrated above, this cannot account for narrower lines observed at lower temperature. A possible explanation for the line-narrowing effect is a reduced motional interference with proton decoupling (Rothwell and Waugh 1981); specifically, as the temperature is lowered, some side chains (or solvent molecules) may undergo a transition from the intermediate- to slow-exchange timescales, thereby reducing the interference with decoupling and improving the observed linewidths. Although this would enhance sensitivity only by about 40% (corresponding to the change in

linewidth), in combination with enhanced CP and (^{13}C-^{13}C) dipolar transfer efficiency, the overall effect on sensitivity for many peaks in the 2D spectrum is quite significant.

In some cases, signal intensity and resolution are compromised at lower temperature, such as in the aromatic region (Fig. 5). Chemical shifts and intensities of aromatic ^{13}C signals depend strongly upon side-chain dynamics, as discussed in previous studies of solid proteins (Franks et al. 2005; McDermott et al. 2000) and known previously from solution NMR studies (Wagner et al. 1976). Specifically we observe at 0°C spin systems consistent with three of the seven aromatic amino acids in AS (F4, Y39, H50, F94, Y125, Y133, Y136). Partial spin systems of the aromatic residues closest to the fibril core are observed, including

Fig. 5 Comparison of aromatic region of CC 2D spectra acquired with different temperatures and DARR mixing times. (**A**) 0°C with 10 ms DARR mixing, (**B**) 0°C with 200 ms mixing, (**C**) –40°C with 10 ms mixing, (**D**) –40°C with 200 ms DARR mixing. Spectra are processed identically, with net line broadening of 0.5 and 0.3 ppm in indirect and direct dimensions, respectively. Experiment times were 9 h for A and C and 42 h for B and D
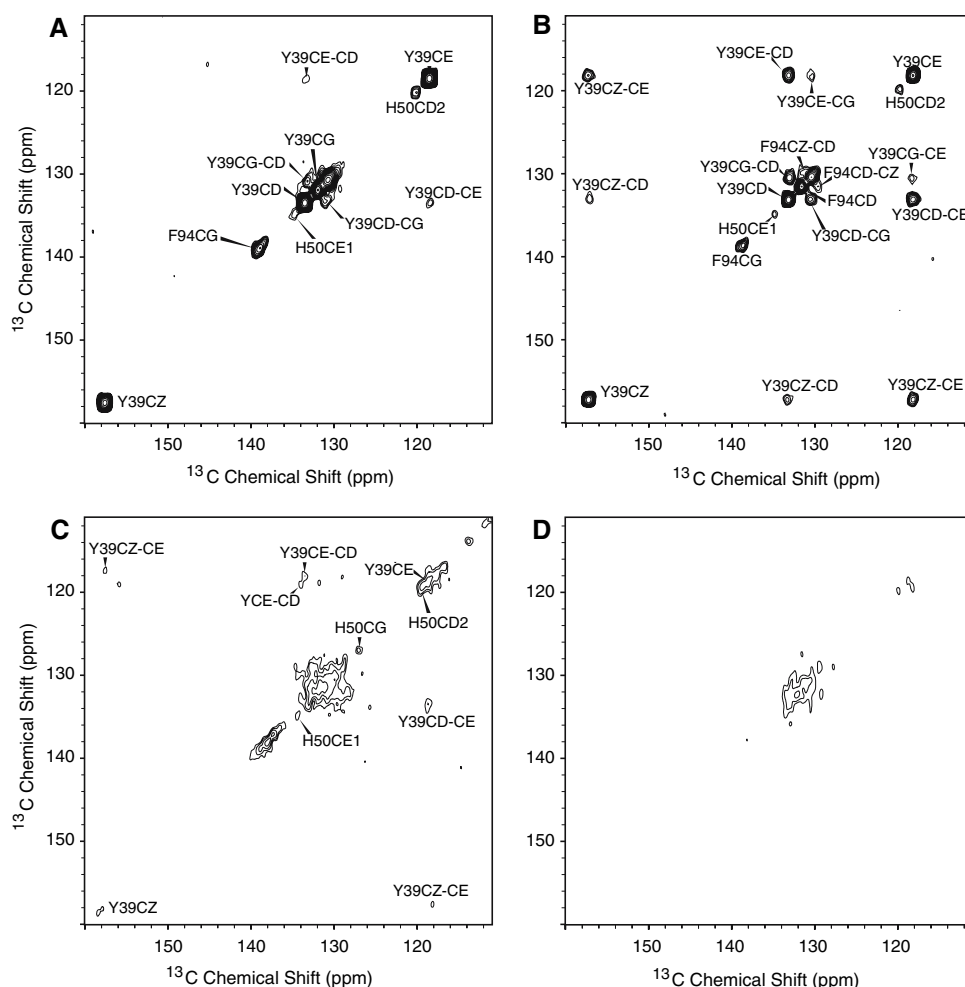
Y39CZ-CZ, F94CG-CG and H50CD2-CD2; however, the only intraresidue crosspeaks observed are Y39CD-CE and Y39CD-CG. Longer homonuclear mixing times, typically used for observation of interresidue crosspeaks, also enhance the intensity of the aromatic ring spin systems. With 200 ms mixing (Fig. 5B), the complete Y39 spin system as well as new F94CD-CZ crosspeaks were observed. The degenerate chemical shifts for the CD1/CD2 and CE1/CE2 of Tyr and Phe residues are consistent with ring flipping in the limit of fast exchange. As temperature is decreased to –40°C, these resonances significantly broaden, some beyond detection (Fig. 5C and D). While resonances are significantly weaker (or not observed at all) in the same region at –40°C, an additional weak Tyr spin system (most likely Y125) is observed just above the noise floor. This line broadening as a function of temperature is consistent with intermediate exchange, which in the case of aromatic rings with typical activation energy barriers is expected in general to occur between room temperature and –50°C, although the precise rates will vary, depending on the details of structure near the aromatic rings, which

remain to be determined (Lewis et al. 1984; Rice et al. 1981, 1987).

Temperature-dependent secondary structure trends

To investigate the distribution of secondary structure within amino acid type, the CC 2D spectra were analyzed by integrating regions of the spectra corresponding to β-sheet, turn/coil and α-helical secondary structure for each uniquely resolved amino acid residue type, using characteristic chemical shift ranges in the BMRB database and the chemical shift index (CSI) of Wishart and Sykes (Wishart and Sykes 1994) (Table 1). For the Ala CA-CB region, at 0°C, 73% of the signals are observed in β-sheets, with only 20% in turns/coil and the remainder (7%) in α-helices. At lower temperatures, the relative distribution of secondary structure changes, apparently due to increases in intensity from non-sheet portions of the molecule (which are expected to be more mobile at the higher temperatures). For example, at –40°C, 51% of the observable residues for

Table 1 Secondary structure analysis of Ala CA-CB cross-peaks based on 2D CC spectra

Temperature (°C)	Region	CA range (ppm)	CB range (ppm)	Integrated intensity (CA-CB cross peaks) (%)	Integrated intensity (CB-CA cross peaks) (%)
0	Ala CA-CB β-sheet	48.5–52.5	20.6–26.5	73	68
0	Ala CA-CB turn/coil	50.5–54.0	15.3–20.7	20	27
0	Ala CA-CB α-helix	54.0–56.7	17.2–20.0	7	5
–20	Ala CA-CB β-sheet	48.5–52.5	20.6–26.5	63	63
–20	Ala CA-CB turn/coil	50.5–54.0	15.3–20.7	25	24
–20	Ala CA-CB α-helix	54.0–56.7	17.2–20.0	12	13
–40	Ala CA-CB β-sheet	48.5–52.5	20.6–26.5	49	51
–40	Ala CA-CB turn/coil	50.5–54.0	15.3–20.7	23	22
–40	Ala CA-CB α-helix	54.0–56.7	17.2–20.0	28	27

WT AS fibrils are found in turn/coil (23%) or helical (28%) conformations. Reproducibility of integration values for multiple data sets acquired on common samples was within ±2%. Similarly high precision was observed in evaluations on both sides of the diagonal, that is, CA-CB (CA in F1 and CB in F2) versus CB-CA (CA in F1 and CB in F2) peaks.

The percentage of secondary structure in AS fibrils was previously determined by Raman spectroscopy (Apetri et al. 2006) to be 28% helix and 66% sheet in mature fibrils, consistent with the percentage of helical secondary structure observed in our samples. However, Raman spectroscopy provides only bulk measurements of the secondary structure, not the type of site-specific or at least residue-specific information available from SSNMR. Thus, with our experimental data, the helix content can be localized based on trends among several amino acid types, such as Ala, Gly, Thr and Val (see further discussion below).

Improved sensitivity at lower temperatures enables confident assignment

Chemical shift assignments were performed with 2D CC and 3D NCACX, NCOCX, CCC, and CANCO experiments. Assignment was greatly facilitated by the improved spectra acquired at lower temperatures (typically –40°C) due to the greater signal intensity and number of resonances present. Partial assignments of the fibril core (approximately residues 60 to 90) and several outlying stretches (L38 to S42, H50 to E57, and A91 to V95) have previously been published, and our data did show modest agreement (several carbon resonances) with this earlier work (Heise et al. 2005); however, due to a significant number of differences and incompleteness of the previously published peak list, we performed our AS assignments entirely de novo. For example, the carbonyl dimension in our NCOCX and NCACX 3Ds experiments

permitted C′ assignments for all core residues, which were largely absent in the previous work. In the assignment strategies employed here, the carbonyl resonances also helped to confirm connectivities between neighboring residues.

Table 2 presents the chemical shift assignments in several categories, corresponding to the degree of confidence in the assignment. Sequence-specific assignments are reported in category one only for cases that could be made with an especially high level of confidence based on the data available. Necessary criteria for inclusion in this list were: (1) observation of complete side-chain chemical shift patterns for amino acids with short side-chains (Gly, Ser, Ala, Thr or Val) or a minimum of N, C', CA, and CB for others; (2) connectivities with common frequencies in at least three of the aforementioned 3D experiments for each resonance, with an agreement within the digital resolution of the respective experiments; (3) confirmation of the presence of all peaks in the 3D spectra with the corresponding peaks expected in the 2D spectra with a minimum signal intensity of five times the root mean squared (RMS) noise threshold; in cases where peaks in the 3D spectra were near the noise threshold, analogous 2D experiments with higher sensitivity were examined to confirm the peaks.

A second category of assignments was made based upon spin systems that were observed in the 2D spectra but did not yield all of the expected cross peaks in the 3D data sets. Therefore complete analysis of the correlation patterns in the 3D spectra was not possible. This reflects the variations in signal intensities throughout the fibril, consistent with the observed 1D spectra above. Nevertheless, based on unique patterns of chemical shifts (especially in the longer mixing time CC data sets), it was possible to identify patterns associated only with particular pairs of amino acid residues, such as A53-T54 and G41-S42. Many other pairs, such as Gly-Ala, Val-Ala and Val-Thr were also identified.

Table 2 Chemical shifts for WT AS fibrils

	N	C'	CA	CB	CG	CD	CE	CZ
Category 1								
T64	114.3	175.2	59.3	70.0				
N65	127.5	173.9	53.8	45.8				
V66	123.5	178.2	60.6	32.8				
G67	109.9	171.9	46.4					
G68	102.0	172.2	43.3					
A69	126.3	175.3	49.8	23.5				
V70	120.8	174.7	60.0	36.2	21.2			
V71	126.2	174.7	60.9	34.9				
T72		175.8	59.7	70.0				
G73	109.0	173.3	44.1					
V74	126.7	175.1	61.1	35.0	19.8			
T75	128.4	171.9	61.7	70.6	21.5			
A76	130.6	174.1	49.7	21.8				
V77	124.2	172.8	60.5	35.9				
A78	130.2	176.0	49.9	25.3				
Q79	120.2	176.2	52.2	32.4	33.0			
K80	122.8	174.0	53.7	33.8				
A85	127.8	174.4	51.7	19.9				
G86	116.6	172.6	48.5					
S87	118.7	172.7	57.4	69.3				
I88	118.4	175.1	59.2	42.5	27.8/17.5	14.5		
A89	129.3	177.2	54.3	18.2				
A90	123.6	174.6	51.3	21.3				
A91	126.2	175.8	49.2	23.7				
T92	125.8	174.5	61.0	70.0				
G93	115.2	169.8	47.6					
Category 2								
T22			67.1	68.5				
V26		174.9	60.9					
A27	133.3	175.2	50.1	21.6				
Y39			57.8	39.0	130.5	133.2	118.3	157.5
G41		173.0	46.4					
S42	122.4	175.6	56.7	65.2				
H50					127.0	119.9	134.8	129.7
V52			59.6	36.2				
A53	128.4	174.1	51.8	15.9				
T54	123.9	173.7	60.3	72.2				
V55			61.2	34.4				
V63		174.8	60.9					
G84		173.2	46.1					
F94			58.0	39.7	138.8	131.6		
A107			50.8	18.0				
I112			59.5	42.1	28.1/18.1	14.7		
S129	112.4	171.1	58.6	67.6				
Category 3								
Ala	120.9	178.7	54.9	19.1				
Ala	123.1	179.1	54.9	17.5				

Table 2 continued

	N	C'	CA	CB	CG	CD	CE	CZ
Ala			55.3	18.5				
Ala	126.3	172.4	50.6	26.0				
Ala	124.4	176.1	55.7	18.3				
Ala			52.2	19.1				
Ala		171.9	52.0	16.9				
Ala			51.0	23.7				
Ala	123.6	174.9	50.2	23.9				
Thr	126.2	172.5	62.3	69.4				
Thr	122.7	172.7	61.6	71.7				
Thr			58.6					
Pro			60.9	32.9	49.9			
Pro			61.7		50.5			
Pro			62.6		50.8			
Pro			63.0		50.4			

A third category of assignments is reported by amino acid type, corresponding to spin systems for which correlation patterns were uniquely consistent with given residue type but could not be linked to neighboring residues due to missing or overlapped signals in the available spectra. The 2D and 3D homonuclear ^{13}C experiments were especially valuable for confirming characteristic chemical shift patterns for each amino acid type.

Regions of AS that could be assigned with high confidence (category one) include two long stretches of amino acids from β-strands in the core of the AS fibril (from 64 to 80 and 85 to 93) that gave particularly strong correlations. A strip plot from the NCACX and NCOCX 3D spectra acquired at –40°C illustrates the criteria for inclusion in this level of analysis (Fig. 6). The secondary structure of the fibril core was analyzed using the chemical shifts to generate likely backbone torsion angles with TALOS (Cornilescu et al. 1999) (Figure 7). This analysis confirmed that the strongest signals, corresponding to residues V70 to Q79, exhibit the signature of β-strand secondary structure. On the N-terminal side of this region are several residues in β-strand conformation (T64 to V66) and then a turn or bulge at G67 (based on the lack of distinctly helical or β-strand chemical shifts for this residue), followed by another β-strand from G68 to G73, although the T72 and G73 crosspeaks are weak relative to the rest of the fibril core which could suggest that these residues participate in a turn or bulge that is more dynamic than the surrounding parts of the fibril. Residues V74 to K80 are consistent with a β-strand conformation. Residues T81 to E83 could not be fully assigned in our 3D experiments due to their depressed intensities; this is likely indicative of a flexible region, possibly a loop, between β-strand components. The next residues (G84-I88) are again in β-strand conformations,

followed by three consecutive Ala residues (A89-A90-A91). The TALOS results and chemical shifts for A89 and A90 are consistent with a compact turn, followed by A91 and T92, which demonstrate β-strand conformation. There is a discontinuity in the TALOS results at G93, which could indicate a hairpin turn or kink, or the general difficulty of accurately predicting Gly conformation from isotropic chemical shifts alone. This is likely a transitional sequence out of the fibrillar core, which is supported by the fact that the majority of the residues further along the sequence from F94 are either not observed or weak relative to the peaks arising from residues in the fibril core. Therefore, the core fibril region from T64 to F94 exhibits chemical shifts consistent with several short β-strands separated by turns of a few residues, as depicted in the schematic model in Fig. 7.

There are no additional long stretches of amino acids that could be assigned with high confidence in our current data sets due to the significant sequence repetitiveness, i.e., the imperfect KTKEGV repeats. Typically the backbone walks were interrupted at Lys or Glu, preventing unambiguous identification of the N-terminal domain. Nevertheless, several short stretches of signals could be assigned into category two, such as V52-A53-T54-V55, providing site-specific insight into the secondary structure of the termini in addition to the fibrillar core. Well-resolved, non-core signal patterns in the spectra most often included Ala, Thr, Ser, and/or Val residues. For example, all of the Ala residues have been assigned at minimum by type by identification of the unambiguous CA-CB signature and additional intraresidue cross peaks found in the NCACX and CCC 3D spectra. Seven of the site-specifically assigned signals (A69, A76, A78, A85, A89, A90, and A91) are in the fibril core. Among the other Ala

Fig. 6 Strip plot illustrating assignment of residues V74 to A78. NCACX and NCOCX spectra were acquired at –40°C. NCACX spectrum was processed with net Lorentzian to Gaussian apodization by 0.4 ppm, 1.0 ppm and 0.8 ppm in F1, F2 and F3, respectively. NCOCX spectrum was processed with net line broadening of 0.6, 1.0, and 0.7 ppm in F1, F2, and F3, respectively
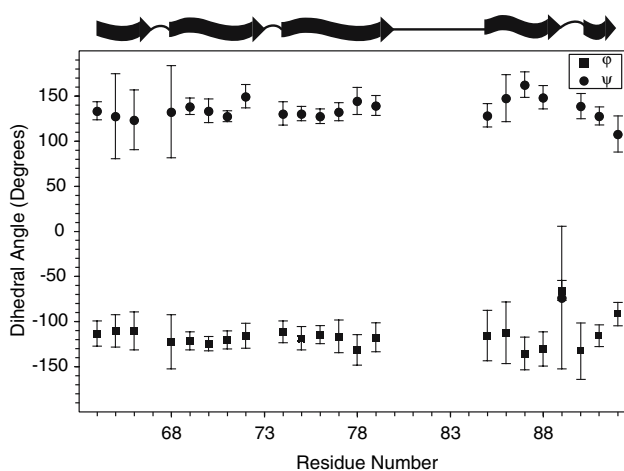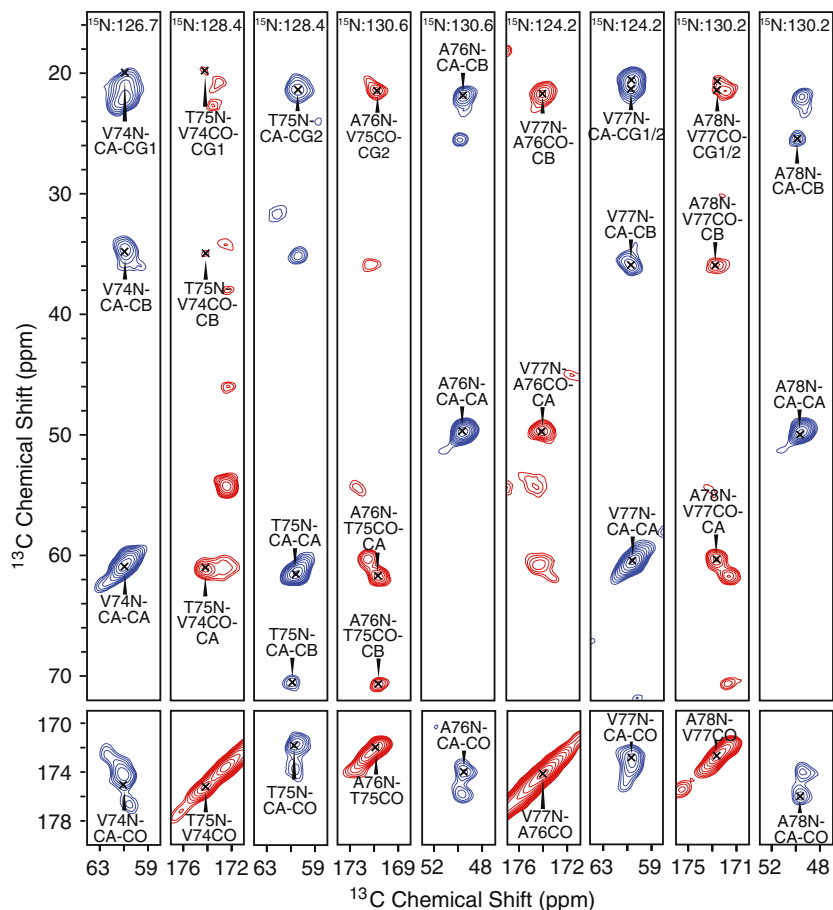

Fig. 7 Secondary structure of AS fibrils from TALOS analysis. The backbone dihedral angles φ ((squares) and ψ (circles) are shown with error bars derived from the 10 best matches to the TALOS database. Above the plot is a cartoon representation of the predicted secondary structure for the fibril core. Likely turn regions or discontinuities in the beta-strands are depicted with a curved line, while the unassigned portion (81–83) is represented with a straight line

residues, three have secondary shifts consistent with a random coil conformation; this is the same number of Ala residues found in the C-terminus (A107, A124, and A140).

A107 precedes P108, accounting for its unusual random coil chemical shifts (50.8, 18.0 ppm), as described in general by Wishart (Wishart et al. 1995) and previously observed in AS by Heise and coworkers (Heise et al. 2005). The remaining Ala signals are located between positions 11 and 56 in the AS sequence. To account for the 30% helical Ala signal, at least four of these seven must be in helical conformations and the remainder in beta or turn conformations. These unassigned N-terminal Ala signals are typically embedded between Lys or other Ala; therefore, site-specific assignments are challenged by the high prevalence of Lys and the similarities of CA and CB chemical shifts for helical Ala.

In contrast to the Ala distribution of secondary structure, most of the Thr residues are in β-strand conformations, including five that were unambiguously assigned (T54, T64, T72, T75, T92) and four others that likely include T81. Thus, the majority of the KTK repeats are β-strands. Short, flexible segments containing Ala, Gly, and/or Val residues likely separate these KTK repeats. For example, the Val CA-CB region exhibits strong helical signal patterns in the lower temperature spectra (Fig. 4I). The Val spin system including the CA at 66.7 ppm and CB at 32 ppm demonstrates signal intensity significantly greater

than anticipated for a single site. In the CC 2D spectrum, several C' signals are observed in the range 176 to 180 ppm, correlated to this unique CA frequency. The 3D CCC spectra further validate the existence of multiple helical Val residues. Likewise, the same CA and CB peaks are correlated to several different ^{15}N frequencies in the 3D NCC experiments. Since the CA, CB, CG1, and CG2 resonance frequencies depend most strongly upon backbone and side-chain conformation (i.e., the $\chi 1$ trans rotameric state), the high degree of overlap among these signals is not surprising. The N and C' frequencies, which depend upon the residue type and conformation of the neighboring residues, show greater dispersion. These helical Val residues must be located in the N-terminal domain, based on the fact that the assigned Val are all β-strand (V66, V70, V71, V74, and V77), and there are only two (V95 and V118) in the C-terminus.

These turn regions throughout the N-terminal domain, consisting primarily of Gly, Ala, and Val residues, have high mobility relative to the central portion of the fibril, as evidenced by the temperature-dependent spectra. Both the overall numbers of signals and their intensities are substantially depressed at higher temperatures, while the majority of the core residues are visible at higher temperatures; this suggests that the N-terminal β-sheet regions are less rigid than those in the fibrillar core, enabled by the numerous turns found at the helical Ala and Val residues.

Conclusion

In this study, we have demonstrated substantial improvements in the sensitivity of SSNMR spectra of hydrated AS fibrils as temperature is lowered. Although the resolution of signals present in the 0 °C spectra is excellent, many peaks are missing; the low signal intensities and lower number of observed peaks is especially apparent in multidimensional ^{13}C-^{13}C and ^{15}N-^{13}C spectra. For example, significantly fewer crosspeaks than expected are observed, due to poor cross polarization efficiency in the mobile domains of the fibril; this problem is exacerbated in experiments requiring multiple cross polarization steps, such as NCOCX and NCACX 3D experiments. In our hands sufficient sensitivity in such 3D experiments could not be obtained at 0 °C on hydrated fibrils.

The presence of substantial molecular dynamics of AS fibrils, especially beyond the fibril core, is consistent with the data obtained by EPR (Der-Sarkissian et al. 2003), SSNMR (Heise et al. 2005), and mass spectrometry analysis of hydrogen exchange in the core (Del Mar et al. 2005). These methods collectively support a model in which a stable, well-ordered fibril core is surrounded by terminal domains that exhibit significant motion. The

motional modes that could contribute to intensity losses at the higher temperature might include: (1) global diffusion of the AS fibril particles, (2) conformational rearrangements within monomeric AS domains, or (3) local side-chain motions. The observation of core signals by several different spectroscopic techniques appears to rule out global diffusion as the primary averaging mechanism of dipolar coupling (i.e., fibril core signals would also be attenuated by this mechanism). Rather, the second and third mechanisms are dominant.

The observation that AS fibrils yield spectra of increased intensity without sacrificing resolution contrasts somewhat with previous SSNMR temperature studies of proteins, such as in GB1 where linewidths broadened and signal intensities decreased between 0 and –50°C (Franks et al. 2005). Likewise, nanocrystalline proteins (Martin and Zilm 2003) and HET-s prion amyloid fibrils (Siemer et al. 2006b) also demonstrated significant broadening in all parts of the sequence as temperature was lowered. Ultimately the behavior of each type of solid protein sample as a function of temperature depends upon the details of molecular dynamics and solvent interactions, and therefore it is not possible to extrapolate the behavior observed here in AS fibrils to other amyloidogenic peptides. Nevertheless, in this case the effects are substantial.

Some regions of the AS spectra, such as the aromatic carbons, do exhibit additional line broadening at lower temperature, which we attribute to specific local conformational dynamic events. A subset of aromatic side chains, such as Tyr, are observed at lower temperatures, indicative of higher activation energy barriers in these residues. These sites follow the more general trend of increasing signal intensity at lower temperatures, highlighting the importance of acquiring spectra over a range of temperatures in order to identify optimal conditions for performing more time-intensive multidimensional experiments. By doing so, we have been able to enhance signal intensity for most residue types throughout AS fibrils. Observation of the majority of residues in the fibril is an important step towards solving the 3D structures of such amyloid species. An atomic-resolution structure of AS fibrils could provide important insight into the pathogenesis of Parkinson's disease as well as potential targets for drug therapies.

References

Apetri MM, Maiti NC, Zagorski MG, Carey PR, Anderson VE (2006) Secondary structure of alpha-synuclein oligomers:

Characterization by Raman and atomic force microscopy. J Mol Biol 355:63–71

Balbach JJ, Ishii Y, Antzutkin ON, Leapman RD, Rizzo NW, Dyda F, Reed J, Tycko R (2000) Amyloid fibril formation by A beta(16–22), a seven-residue fragment of the Alzheimer's beta-amyloid peptide, and structural characterization by solid state NMR. Biochemistry 39:13748–13759

Balbach JJ, Petkova AT, Oyler NA, Antzutkin ON, Gordon DJ, Meredith SC, Tycko R (2002) Supramolecular structure in full-length Alzheimer's beta-amyloid fibrils: Evidence for a parallel beta-sheet organization from solid-state nuclear magnetic resonance. Biophys J 83:1205–1216

Baldus M, Petkova AT, Herzfeld JH, Griffin RG (1998) Cross polarization in the tilted frame: assignment and spectral simplification in heteronuclear spin systems. Mol Phys 95:1197–1207

Bennett AE, Rienstra CM, Auger M, Lakshmi KV, Griffin RG (1995) Heteronuclear decoupling in rotating solids. J Chem Phys 103:6951–6958

Benzinger TLS, Gregory DM, Burkoth TS, Miller-Auer H, Lynn DG, Botto RE, Meredith SC (2000) Two-dimensional structure of beta-amyloid(10–35) fibrils. Biochemistry 39:3491–3499

Benzinger TLS, Gregory DM, Burkoth TS, Miller-Auer H, Lynn DG, Botto RE, Meredith SC (1998) Propagating structure of Alzheimer's beta-amyloid ((10–35)) is parallel beta-sheet with residues in exact register. Proc Natl Acad Sci USA 95:13407–13412

Castellani F, van Rossum B, Diehl A, Schubert M, Rehbein K, Oschkinat H (2002) Structure of a protein determined by solid-state magic-angle-spinning NMR spectroscopy. Nature 420:98–102

Conway KA, Harper JD, Lansbury PT (2000) Fibrils formed in vitro from alpha-synuclein and two mutant forms linked to Parkinson's disease are typical amyloid. Biochemistry 39:2552–2563

Cornilescu G, Delaglio F, Bax A (1999) Protein backbone angle restraints from searching a database for chemical shift and sequence homology. J Biomol NMR 13:289–302

Delaglio F, Grzesiek S, Vuister GW, Zhu G, Pfeifer J, Bax A (1995) Nmrpipe – a multidimensional spectral processing system based on Unix pipes. J Biomol NMR 6:277–293

Del Mar C, Greenbaum EA, Mayne L, Englander SW, Woods VL (2005) Structure and properties of alpha-synuclein and other amyloids determined at the amino acid level. Proc Natl Acad Sci USA 102:15477–15482

Der-Sarkissian A, Jao CC, Chen J, Langen R (2003) Structural organization of alpha-synuclein fibrils studied by site-directed spin labeling. J Biol Chem 278:37530–37535

Franks WT, Zhou DH, Wylie BJ, Money BG, Graesser DT, Frericks HL, Sahota G, Rienstra CM (2005) Magic-angle spinning solid-state NMR spectroscopy of the beta 1 immunoglobulin binding domain of protein G (GB1): 15N and 13C chemical shift assignments and conformational analysis. J Am Chem Soc 127:12291–12305

Frericks HL, Zhou DH, Yap LL, Gennis RB, Rienstra CM (2006) Magic-angle spinning solid-state NMR of a 144 kDa membrane protein complex: E-coli cytochrome bo(3) oxidase. J Biomol NMR 36:55–71

Goddard TD, Kneller DG (2006), Sparky 3.112 University of California, San Francisco

Hartmann SR, Hahn EL (1962) Nuclear double resonance in the rotating frame. Phys Rev 128:2042

Hediger S, Meier BH, Ernst RR (1995) Adiabatic passage Hartmann-Hahn cross-polarization in NMR under magic-angle sample-spinning. Chem Phys Lett 240:449–456

Heise H, Hoyer W, Becker S, Andronesi OC, Riedel D, Baldus M (2005) Molecular-level secondary structure, polymorphism, and dynamics of full-length alpha-synuclein fibrils studied by solid-state NMR. Proc Natl Acad Sci USA 102:15871–15876

Igumenova TI, Wand AJ, McDermott AE (2004) Assignment of the backbone resonances for microcrystalline ubiquitin. J Am Chem Soc 126:5323–5331

Iwai A, Yoshimoto M, Masliah E, Saitoh T (1995) Non-a-beta component of Alzheimers-disease amyloid (Nac) is amyloidogenic. Biochemistry 34:10139–10145

Kloepper KD, Woods WS, Winter KA, George JM, Rienstra CM (2006) Preparation of alpha-synuclein fibrils for solid-state NMR: Expression, purification, and incubation of wild-type and mutant forms. Protein Expr Purif 48:112–117

Kruger R, Kuhn W, Muller T, Woitalla D, Graeber M, Kosel S, Przuntek H, Epplen JT, Schols L, Riess O (1998) Ala30Pro mutation in the gene encoding alpha-synuclein in Parkinson's disease. Nat Genet 18:106–108

Lange A, Becker S, Seidel K, Giller K, Pongs O, Baldus M (2005) A concept for rapid protein-structure determination by solid-state NMR spectroscopy. Angew Chem Int Ed 44:2089–2092

Lansbury PT, Costa PR, Griffiths JM, Simon EJ, Auger M, Halverson KJ, Kocisko DA, Hendsch ZS, Ashburn TT, Spencer RGS, Tidor B, Griffin RG (1995) Structural model for the beta-amyloid fibril based on interstrand alignment of an antiparallel-sheet comprising a c-terminal peptide. Nat Struct Biol 2:990–998

Lewis BA, Rice DM, Olejniczak ET, Dasgupta SK, Herzfeld J, Griffin RG (1984) Deuterium NMR studies of molecular dynamics in bacteriorhodopsin - analysis of lineshapes and intensities for phenylalanine, tyrosine, and leucine sidechains. Biophys J 45:A213–A213

Li Y, Wylie BJ, Rienstra CM (2006) Selective refocusing pulses in magic-angle spinning NMR: Characterization and applications to multidimensional protein spectroscopy. J Magn Reson 179:206–216

Li Y, Berthold DA, Frericks HL, Gennis RB, Rienstra CM (2007) Partial 13C and 15N chemical shift assignments of the disulfide bond forming enzyme DsbB by 3D magic-angle spinning NMR spectroscopy. Chembiochem 5:434–42

Marion D, Wuthrich K (1983) Application of phase sensitive two-dimensional correlated spectroscopy (Cosy) for measurements of 1H-1H spin-spin coupling-constants in proteins. Biochem Biophys Res Commun 113:967–974

Martin RW, Zilm KW (2003) Preparation of protein nanocrystals and their characterization by solid state NMR. J Magn Reson 165:162–174

McDermott A, Polenova T, Bockmann A, Zilm KW, Paulsen EK, Martin RW, Montelione GT (2000) Partial NMR assignments for uniformly (13C, 15N)-enriched BPTI in the solid state. J Biomol NMR 16:209–219

Miake H, Mizusawa H, Iwatsubo T, Hasegawa M (2002) Biochemical characterization of the core structure of alpha-synuclein filaments. J Biol Chem 277:19213–19219

Morcombe CR, Gaponenko V, Byrd RA, Zilm KW (2004) Diluting abundant spins by isotope edited radio frequency field assisted diffusion. J Am Chem Soc 126:7196–7197

Morcombe CR, Zilm KW (2003) Chemical shift referencing in MAS solid state NMR. J Magn Reson 162:479–486

Petkova AT, Ishii Y, Balbach JJ, Antzutkin ON, Leapman RD, Delaglio F, Tycko R (2002) A structural model for Alzheimer's beta-amyloid fibrils based on experimental constraints from solid state NMR. Proc Natl Acad Sci USA 99:16742–16747

Petkova AT, Leapman RD, Guo ZH, Yau WM, Mattson MP, Tycko R (2005) Self-propagating, molecular-level polymorphism in Alzheimer's beta-amyloid fibrils. Science 307:262–265

Petkova AT, Yau WM, Tycko R (2006) Experimental constraints on quaternary structure in Alzheimer's beta-amyloid fibrils. Biochemistry 45:498–512

Petkova AT, Tycko R (2004) Rotational resonance in uniformly 13C-labeled solids: effects on high-resolution magic-angle spinning

NMR spectra and applications in structural studies of biomolecular systems. J Magn Reson 168:137–146

Pines A, Gibby MG, Waugh JS (1973) Proton-enhanced NMR of dilute spins in solids. J Chem Phys 59:569–590

Polymeropoulos MH, Lavedan C, Leroy E, Ide SE, Dehejia A, Dutra A, Pike B, Root H, Rubenstein J, Boyer R, Stenroos ES, Chandrasekharappa S, Athanassiadou A, Papapetropoulos T, Johnson WG, Lazzarini AM, Duvoisin RC, DiIorio G, Golbe LI, Nussbaum RL (1997) Mutation in the alpha-synuclein gene identified in families with Parkinson's disease. Science 276:2045–2047

Rice DM, Wittebort RJ, Griffin RG, Meirovitch E, Stimson ER, Meinwald YC, Freed JH, Scheraga HA (1981) Rotational jumps of the tyrosine side-chain in crystalline enkephalin – 2H NMR lineshapes for aromatic ring motion in solids. J Am Chem Soc 103:7707–7710

Rice DM, Meinwald YC, Scheraga HA, Griffin RG (1987) Tyrosyl motion in peptides – 2H NMR lineshapes and spin-lattice relaxation. J Am Chem Soc 109:1636–1640

Rienstra CM, Hohwy M, Hong M, Griffin RG (2000) 2D and 3D 15N-13C-13C NMR chemical shift correlation spectroscopy of solids: Assignment of MAS spectra of peptides. J Am Chem Soc 122:10979–10990

Ritter C, Maddelein ML, Siemer AB, Luhrs T, Ernst M, Meier BH, Saupe SJ, Riek R (2005) Correlation of structural elements and infectivity of the HET-s prion. Nature 435:844–848

Rothwell WP, Waugh JS (1981) Transverse relaxation of dipolar coupled spin systems under Rf-Irradiation – Detecting motions in solids. J Chem Phys 74:2721–2732

Schaefer J, Stejskal EO (1976) 13C-NMR of polymers spinning at the magic angle. J Am Chem Soc 98:1031

Serpell LC, Berriman J, Jakes R, Goedert M, Crowther RA (2000) Fiber diffraction of synthetic alpha-synuclein filaments shows amyloid-like cross-beta conformation. Proc Natl Acad Sci USA 97:4897–4902

Siemer AB, Ritter C, Ernst M, Riek R, Meier BH (2005) High-resolution solid-state NMR spectroscopy of the prion protein HET-s in its amyloid conformation. Angew Chem Int Ed 44:2441–2444

Siemer AB, Arnold AA, Ritter C, Westfeld T, Ernst M, Riek R, Meier BH (2006a) Observation of highly flexible residues in amyloid fibrils of the HET-s prion. J Am Chem Soc 128:13224–13228

Siemer AB, Ritter C, Steinmetz MO, Ernst M, Riek R, Meier BH (2006b) 13C, 15N resonance assignment of parts of the HET-s prion protein in its amyloid form. J Biomol NMR 34:75–87

Spillantini MG, Schmidt ML, Lee VMY, Trojanowski JQ, Jakes R, Goedert M (1997) alpha-synuclein in Lewy bodies. Nature 388:839–840

Takegoshi K, Nakamura S, Terao T (2001) 13C-1H dipolar-assisted rotational resonance in magic-angle spinning NMR. Chem Phys Lett 344:631–637

Van Geet AL (1968) Calibration of the methanol and glycol nuclear magnetic resonance thermometers with a static thermistor probe. Anal Chem 40:2227–2229

Wagner G, DeMarco A, Wüthrich K (1976) Dynamics of the aromatic amino acid residues in the globular conformation of the basic pancreatic trypsin inhibitor (BPTI). I 1H NMR studies Biophys Struct Mech 2:139–158

Wishart DS, Bigam CG, Holm A, Hodges RS, Sykes BD (1995) 1H, 13C, and 15N random coil NMR chemical-shifts of the common amino acids .1. Investigations of nearest-neighbor effects. J Biomol NMR 5:67–81

Wishart DS, Sykes BD (1994) Chemical shifts as a tool for structure determination. Methods Enzymol 239:363–392

Zarranz JJ, Alegre J, Gomez-Esteban JC, Lezcano E, Ros R, Ampuero I, Vidal L, Hoenicka J, Rodriguez O, Atares B, Llorens V, Tortosa EG, del Ser T, Munoz DG, de Yebenes JG (2004) The new mutation, E46K, of alpha-synuclein causes Parkinson and Lewy body dementia. Ann Neurol 55:164–173

Zech SG, Wand AJ, McDermott AE (2005) Protein structure determination by high-resolution solid-state NMR spectroscopy: Application to microcrystalline ubiquitin. J Am Chem Soc 127:8618–8626

Zhao X, Eden M, Levitt MH (2001) Recoupling of heteronuclear dipolar interactions in solid-state NMR using symmetry-based pulse sequences. Chem Phys Lett 342:353–361

Zhou DH, Kloepper KD, Winter KA, Rienstra CM (2006) Band-selective C-13 homonuclear 3D spectroscopy for solid proteins at high field with rotor-synchronized soft pulses. J Biomol NMR 34:245–257